

**Tapering of the interventricular septum can affect ultrasound shear wave elastography
An in vitro and in silico study**

Sabbadini, A.; Caenen, A.; Keijzer, L. B.H.; van Neer, P. L.M.J.; Vos, H. J.; de Jong, N.; Verweij, M. D.

DOI

[10.1121/10.0005646](https://doi.org/10.1121/10.0005646)

Publication date

2021

Document Version

Final published version

Published in

Journal of the Acoustical Society of America

Citation (APA)

Sabbadini, A., Caenen, A., Keijzer, L. B. H., van Neer, P. L. M. J., Vos, H. J., de Jong, N., & Verweij, M. D. (2021). Tapering of the interventricular septum can affect ultrasound shear wave elastography: An in vitro and in silico study. *Journal of the Acoustical Society of America*, *150*(1), 428-440. <https://doi.org/10.1121/10.0005646>

Important note

To cite this publication, please use the final published version (if applicable).
Please check the document version above.

Copyright

Other than for strictly personal use, it is not permitted to download, forward or distribute the text or part of it, without the consent of the author(s) and/or copyright holder(s), unless the work is under an open content license such as Creative Commons.

Takedown policy

Please contact us and provide details if you believe this document breaches copyrights.
We will remove access to the work immediately and investigate your claim.

Tapering of the interventricular septum can affect ultrasound shear wave elastography: An *in vitro* and *in silico* study

A. Sabbadini, A. Caenen, L. B. H. Keijzer, P. L. M. J. van Neer, H. J. Vos, N. de Jong, and M. D. Verweij

Citation: *The Journal of the Acoustical Society of America* **150**, 428 (2021); doi: 10.1121/10.0005646

View online: <https://doi.org/10.1121/10.0005646>

View Table of Contents: <https://asa.scitation.org/toc/jas/150/1>

Published by the [Acoustical Society of America](#)

ARTICLES YOU MAY BE INTERESTED IN

[Accelerating frequency-domain numerical methods for weakly nonlinear focused ultrasound using nested meshes](#)

The Journal of the Acoustical Society of America **150**, 441 (2021); <https://doi.org/10.1121/10.0005655>

[Deep perceptual embeddings for unlabelled animal sound events](#)

The Journal of the Acoustical Society of America **150**, 2 (2021); <https://doi.org/10.1121/10.0005475>

[Double-strand breaks in genome-sized DNA caused by megahertz ultrasound](#)

The Journal of the Acoustical Society of America **150**, 241 (2021); <https://doi.org/10.1121/10.0005539>

[Adult perception of stop consonant voicing in American-English-learning toddlers: Voice onset time and secondary cues](#)

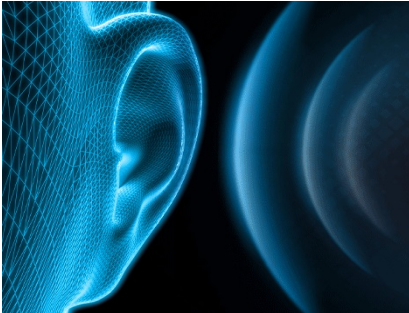
The Journal of the Acoustical Society of America **150**, 460 (2021); <https://doi.org/10.1121/10.0005595>

[Reflections on “Parametric acoustic array,” source of virtual-array sonars](#)

The Journal of the Acoustical Society of America **150**, R1 (2021); <https://doi.org/10.1121/10.0005487>

[A recursive approach for aeroacoustic phased array measurements in wind tunnels](#)

The Journal of the Acoustical Society of America **150**, 417 (2021); <https://doi.org/10.1121/10.0005543>



JASA
THE JOURNAL OF THE
ACOUSTICAL SOCIETY OF AMERICA

SPECIAL ISSUE:
Noise-Induced Hearing Disorders:
Clinical and Investigational Tools

SUBMIT TODAY!

Tapering of the interventricular septum can affect ultrasound shear wave elastography: An *in vitro* and *in silico* study

A. Sabbadini,^{1,a)} A. Caenen,^{2,b)} L. B. H. Keijzer,² P. L. M. J. van Neer,^{3,c)} H. J. Vos,^{2,d)} N. de Jong,^{1,e)} and M. D. Verweij^{1,f)}

¹Applied Sciences, Delft University of Technology, Lorentzweg 1, Delft, 2628 CJ, The Netherlands

²Biomedical Engineering, Department of Cardiology, Erasmus MC, University Medical Center Rotterdam, Doctor Molewaterplein 40, Rotterdam, 3015 GD, The Netherlands

³Ultrasonie Lab, Nederlandse Organisatie voor Toegepast Natuurwetenschappelijk Onderzoek, Oude Waalsdorperweg 63, Den Haag, 2597 AK, The Netherlands

ABSTRACT:

Shear wave elastography (SWE) has the potential to determine cardiac tissue stiffness from non-invasive shear wave speed measurements, important, e.g., for predicting heart failure. Previous studies showed that waves traveling in the interventricular septum (IVS) may display Lamb-like dispersive behaviour, introducing a thickness-frequency dependency in the wave speed. However, the IVS tapers across its length, which complicates wave speed estimation by introducing an additional variable to account for. The goal of this work is to assess the impact of tapering thickness on SWE. The investigation is performed by combining *in vitro* experiments with acoustic radiation force (ARF) and 2D finite element simulations, to isolate the effect of the tapering curve on ARF-induced and natural waves in the heart. The experiments show a 11% deceleration during propagation from the thick to the thin end of an IVS-mimicking tapered phantom plate. The numerical analysis shows that neglecting the thickness variation in the wavenumber-frequency domain can introduce errors of more than 30% in the estimation of the shear modulus, and that the exact tapering curve, rather than the overall thickness reduction, determines the dispersive behaviour of the wave. These results suggest that septal geometry should be accounted for when deriving cardiac stiffness with SWE.

© 2021 Acoustical Society of America. <https://doi.org/10.1121/10.0005646>

(Received 26 January 2021; revised 29 June 2021; accepted 30 June 2021; published online 20 July 2021)

[Editor: Guillaume Haiat]

Pages: 428–440

I. INTRODUCTION

Shear wave elastography (SWE) has been the subject of research for some time now because of its potential to improve clinical diagnoses by non-invasively determining tissue stiffness^{1–3} in radiology. In particular, SWE could have important applications in the field of cardiac imaging^{4–8} as a way to assess the stiffness of the heart muscle, which has been identified as a relevant parameter in the diagnosis of heart failure.^{9,10}

In cardiac ultrasound SWE, waves are typically tracked along the interventricular septum (IVS), and can have two different excitation sources: either they are generated by the natural physiology of the heart, e.g., valve closure,^{7,11–14} or

they are generated by an external source, such as acoustic radiation force (ARF).^{15–18} After wave excitation, the waves are recorded using high frame rate imaging, and their propagation pattern in the time domain is used to extract their propagation speed. Under idealized conditions (i.e., in a bulk, purely elastic, time-invariant, linear, and isotropic material), the speed of a shear wave is proportional to the shear modulus of the medium, following the relation

$$G = \rho c_s^2, \quad (1)$$

where ρ is the density of mass (in kg/m³), c_s is the bulk shear speed (in m/s), and G is the shear modulus (in Pa).

However, the IVS is far from these idealized conditions, and waves traveling along the plate-like heart wall show a dispersive behaviour similar to that of Lamb waves.^{4,19–22} These are waves characterized by two infinite sets of guided modes (symmetric and antisymmetric) that propagate with speeds dependent not only on the shear modulus, but also on the thickness of the medium and the frequency of the waves themselves.²³ Moreover, when a plate is loaded by a fluid (as is the case with the IVS, which separates the two blood-filled ventricles), the dispersive behaviour also depends on the properties of that fluid,^{23,24} further complicating the relation between wave speed and muscle stiffness. Varying

^{a)}Electronic mail: a.sabbadini@tudelft.nl, ORCID: 0000-0003-0723-6537.

^{b)}Also at: IBI-Tech-bioMMeda, Gent University, Corneel Heymanslaan 10, Gent, B-9000, Belgium.

^{c)}Also at: Applied Sciences, Delft University of Technology, The Netherlands, ORCID: 0000-0003-4199-4374.

^{d)}Also at: Applied Sciences, Delft University of Technology, The Netherlands.

^{e)}Also at: Biomedical Engineering, Department of Cardiology, Erasmus MC, University Medical Center Rotterdam, The Netherlands.

^{f)}Also at: Biomedical Engineering, Department of Cardiology, Erasmus MC, University Medical Center Rotterdam, The Netherlands, ORCID: 0000-0002-7441-7218.

thickness of the IVS could further affect wave propagation speed, and might be one of the underlying causes for the large reported variability of shear wave speeds in literature on healthy volunteers: natural shear wave studies report speeds with differences of up to 60% between studies^{8,25} and up to 20% within individual works,⁸ while studies employing acoustic radiation force can show inter- and intra-study differences of 60%.^{17,18}

Efforts have been made in the cardiac SWE field to account for the dispersive behaviour of the wave in the material characterization algorithms. Instead of studying the wave propagation characteristics in the space-time ($x-t$) domain, various studies^{4,19,20,26,27} have analysed waves in the frequency-wavenumber ($f-k$) domain to reconstruct the dispersion curves. When approaching the IVS as a fluid-loaded elastic plate, the shear modulus can be extracted by fitting a theoretical Lamb wave dispersion curve to the experimental ones. The advantage of this approach is that the dispersion curves allow one to directly retrieve the bulk shear speed of a medium rather than the dispersive propagation speed in a plate. The first can be easily translated into the stiffness via Eq. (1), while the latter cannot. In fact, it was shown for ARF-based SWE in flat²⁸ and curved plates²⁶ that space-time analyses based on Eq. (1) could underestimate the shear modulus, while analysis in the frequency-wavenumber domain yielded more accurate values of the shear modulus, compared to mechanical elasticity tests.

An underlying assumption of the dispersion curve analysis is that the thickness of the plate is constant. However, it is generally known that the cardiac wall thickness can vary by up to a factor 3 from the equatorial point to the apex in healthy volunteers, with values reported around 8–10 mm and 1–3 mm, respectively,^{29,30} and this variation could be even more dramatic in hypertrophic patients.³¹ Thickness variations are expected to have a significant impact on the propagation of guided waves due to their dependency on the frequency-thickness product, which is especially strong at lower frequencies for zero-order modes. In fact, it has already been shown that, when the slowly varying thickness of a waveguide reaches the frequency-thickness cut-off of a certain mode, mode conversion and reflections take place.^{32–34} Interestingly, natural and ARF-generated waves are expected to be affected differently by the thickness variation, due to their different frequency contents (up to around 150 Hz and 1000 Hz, respectively^{19,22,27,28}).

To the best of our knowledge, the effects of cardiac thickness variations on shear wave propagation characteristics have not been studied yet. The goal of this work is to determine if and how the natural IVS thickness variations could affect cardiac SWE measurements. Therefore, to untangle the complex relationship between wave properties and myocardial material characteristics, we isolated the effects of geometry by studying an elastic plate with varying thickness using numerical simulations and experiments. The experiments were analysed in space-time domain and were used as a proof-of-principle to show that the speed of the waves typically used in SWE varies along the tapered plate.

They also served for validation purposes of our simulation settings; the numerical settings were further verified by comparing quantitatively the simulation results in a flat fluid-loaded plate to the theoretical Lamb wave propagation. The simulations allowed a greater degree of flexibility in modelling different excitation sources and geometries: the effects of geometry on both natural and ARF-induced waves were studied in space-time as well as in frequency-wavenumber domain, and it was possible to assess whether the waves are affected only by the total amount of thickness reduction, or rather depend on the specific tapering curve.

II. METHODS

A. Experimental setup

To isolate the effects of tapering on wave propagation, a polyvinyl alcohol tissue-mimicking phantom was created following the recipe in Ref. 35. A mould was shaped to produce a phantom plate with a tapered section: 12 cm long, 5 cm wide and with thickness varying between 9 and 3 mm.²⁹ In terms of geometry, the phantom can be schematically divided into three sections, each 4 cm long: first, a flat section with a constant thickness of 9 mm, followed by a section in which the thickness decreases linearly from 9 to 3 mm, and, finally, another flat section with a constant thickness of 3 mm [see Fig. 1(a)]. The flat sections of the phantom served two purposes: they extended the propagation medium, reducing boundary effects at the edges of the tapered section, and they provided flat regions of the same sample that were used to obtain reference measurements. The phantom was then entirely submerged in a water tank to simulate the blood that surrounds the IVS. The plate was held in position halfway across the depth of the water tank by 3D printed supports, ensuring that the central section of the sample was loaded by water on both sides and the sample would not float [see Fig. 1(b)].

SWE measurements were performed using a P4–2 probe (ATL, Bothell, Washington, U.S.) connected to a Verasonics Vantage 256 research platform (Verasonics, Kirkland, WA, U.S.). A wave was generated in the centre of the phantom by focusing a push pulse with frequency of 2 MHz, F-number of 1.9, duration of 400 μ s, and a focus depth of 40 mm. After wave generation, the probe switched into tracking mode to record the traveling wave for 20.2 ms using high frame rate imaging with plane wave compounding ($-7^\circ, 0^\circ, 7^\circ$) resulting in an effective frame rate of 3223.5 Hz.

B. Experimental data analysis

Analytic data were obtained by beamforming the radio frequency (RF) data using the Verasonics software. One-lag autocorrelation³⁶ was applied to the IQ-data to obtain the axial particle velocity field. Before calculating the phase differences, the tissue velocity data were smoothed with a Gaussian spatial smoothing filter with total sigma-widths of 0.47° in the azimuthal direction by 0.5 mm in the axial direction. The obtained velocity matrix has a temporal

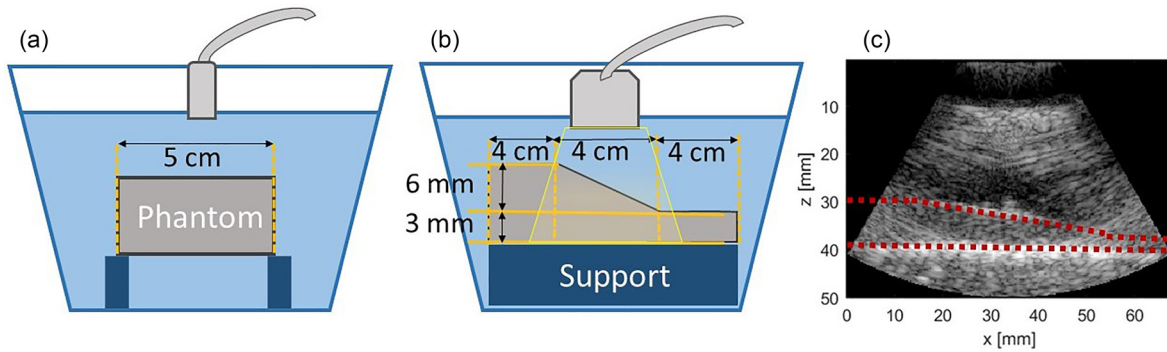


FIG. 1. (Color online) Schematic representation of the experimental setup. (a) Rear view, (b) side view, (c) B-mode image, where the phantom boundaries are highlighted by the red dashed line. The phantom (in light gray) consists of a 4 cm long, 9 mm thick flat section, followed by a 4 cm long section that tapers from 9 to 3 mm, and ends in another 4 cm long flat section, 3 mm thick. 3D printed supports (dark blue) held the phantom halfway through the depth of the tank, while allowing the central section of the plate to be loaded by water on both sides.

resolution of 0.3 ms, and a spatial resolution of 0.24 mm in both the lateral (x) and axial (z) direction. All post-processing was performed using MATLAB R2018b (MathWorks, Natick, MA, U.S.).

Particle velocity data in the z direction was extracted along nine M-lines (virtual lines of receivers) approximately 2 cm long, which were placed at a depth of 10% to 50% of the phantom thickness with respect to its top surface, in increments of 5%. The velocity data in the lower half of the phantom had too low signal-to-noise ratio (SNR) and was therefore excluded from shear wave speed analysis. The extracted data along each line was then spatially up-sampled to a spacing of 0.015 mm. As the ARF was applied in the centre of the x direction, a left and right propagating shear wave was observed. The space-time trajectories of both waves were subsequently analysed by means of a Radon sum algorithm³⁷ to determine their slopes, which correspond

to wave propagation velocities. The difference in speed of the left- and right-propagating waves was calculated for all the m-lines. The average and standard deviation of the speed differences were then computed and used to compare wave propagation in the flat and the tapered sections.

C. Numerical configuration

The numerical model was implemented in Abaqus CAE (Abaqus Inc., Providence, RI, U.S.) using the finite element method (FEM), which has already been extensively used for modelling ARF-based SWE in biological tissue^{38–40} and for waves in curved plates.²⁶ Similar to the experimental geometry, the IVS was modelled as a 2D plate under plane strain assumption, with its thickness tapering linearly from 9 to 3 mm²⁴ and a length of 4 cm, as shown in Fig. 2. Symmetric boundary conditions were applied in the x -direction to the

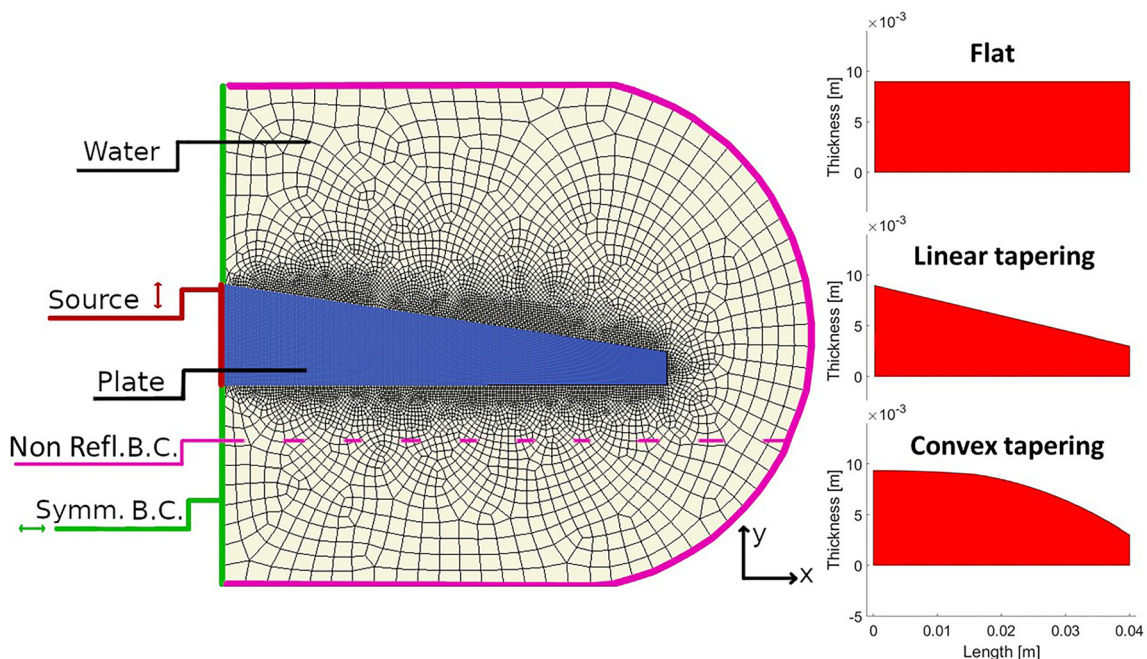


FIG. 2. (Color online) The simulation setup. On the left the numerical FE model is shown, with the plate highlighted in blue and the water in gray. The top right image depicts the 9 mm thick flat plate, below which is shown the plate with linear tapering and, at the bottom, the plate with convex tapering.

left side of the plate in Fig. 2 to avoid boundary effects on the wave excitation. The other sides of the plate were surrounded by a 4 cm thick layer of water, the motion of which was coupled to that of the plate through tie-constraints. The outer boundaries of the water were modelled with non-radiating boundary conditions, to prevent reflections of the outgoing waves. In this model, the plate was described as an isotropic nearly incompressible elastic material with a density ρ of 1045 kg/m³,²⁶ a Poisson's ratio $\nu = 0.49999$,⁴¹ and a Young's modulus of $E = 9$ kPa,¹⁸ to represent the cardiac muscle in its diastolic phase. This corresponds to a shear modulus of 3 kPa and thus a bulk shear speed of 1.69 m/s. The water was modelled as an acoustic medium, with a bulk modulus of 2.2 GPa and a density of 1000 kg/m³, corresponding to a bulk compressional wave speed of 1483 m/s.

The plate was modelled with quadrilateral elements with a length and thickness of 0.2 mm (in the flat plate) or length of 0.2 mm and thickness between 0.2 and 0.07 mm (for the tapered plates). Based on the bulk shear speed, these mesh sizes resulted in frequencies up to 600 Hz being sampled with at least 15 points per wavelength. The solution computed by Abaqus was then sampled with a temporal resolution of 0.038 ms, corresponding to at least 43 samples per period in the frequency range mentioned. To reduce computation time, the water domain was meshed with quadrilateral elements with length and thickness of 0.2 mm only in proximity of the plate domain. The mesh size was then allowed to increase up to 2 mm at the outer boundaries of the water domain (see also Fig. 2).

Natural and ARF waves were simulated by applying a Gaussian-shaped velocity pulse in the transversal direction at the left edge of the plate (see Fig. 2), with peak amplitudes of 2 cm/s. The pulse simulating natural waves had a total duration of 10 ms, while the ARF wave was simulated with a 2 ms pulse, corresponding to full-width half-maximum frequency contents of around 100 Hz and 500 Hz, respectively.

The wave propagation was simulated for a total duration of 40 ms, which is long enough for one pulse to be excited and reach the opposite side of the plate. The simulations were run using an explicit solver.

D. Numerical model validation

The model validation of the numerical model consisted of two steps. First, the chosen numerical settings of our FEM model were verified for a fluid-loaded tissue-mimicking plate by comparing the dispersion characteristics of the simulated ARF wave to those of theoretical Lamb waves. For this purpose, we considered a 4 cm long plate with a constant thickness of 9 mm, surrounded by water, as illustrated in the top right panel of Fig. 2. The material properties of plate and water were the same as described in Sec. II C. The theoretical A0 curve was calculated with the equation for soft tissue mimicking plates in blood,²⁴

$$4k_L^3 \beta \cosh(k_L h) \sinh(\beta h) - (k_s^2 - 2k_L^2)^2 \sinh(k_L h) \cosh(\beta h) = k_s^4 \cosh(k_L h) \cosh(\beta h), \quad (2)$$

where $k_L = \omega/c_L$ is the Lamb wave number, c_L is the frequency dependent Lamb wave velocity, $k_s = \omega/c_s$ is the shear wave number, c_s is the bulk shear wave speed, $\beta = \sqrt{k_L^2 - k_s^2}$, and h is half the thickness of the plate.

The A0 mode was chosen for validation because the employed source generated mainly antisymmetric modes, and because the zeroth-order mode is present at all frequencies, thus yielding more data for comparison with a theoretical curve.

Second, a more qualitative validation of our FEM model was performed with the tapered plate model, described in Sec. II C, by analysing the simulated ARF wave in space-time, as well as the speed difference between left and right halves of the M-lines, in comparison to the experimental ones. The duration of the pulse used in the simulations of this validation step was 5 ms, corresponding to a full-width half-maximum frequency content of around 250 Hz, to better match our experimental data.

E. Numerical data analysis

The simulated data were processed in MATLAB. A 2.5 cm long M-line was positioned at a depth of 10% of the plate thickness. The M-line was drawn 1 cm away from the left edge of the model (where the source is applied), in order to reduce the effects of proximity to the source.⁴² The particle velocity data were then interpolated from the FEM-grid to an equidistant grid with 0.05 mm spacing along each M-line. Distances were consequently measured along the M-lines. The simulated wave propagated from one end of the plate to the other, thus providing a single, one-directional propagation branch. To observe possible decelerations, therefore, the propagation path was split into two halves (the first comprising of the wave traveling from the left edge of the plate to the centre, the second encompassing the propagation from the centre to the right end), and each half was analysed with the Radon sum algorithm separately.

For the wave analysis in the frequency-wavenumber domain, the space-time velocity data recorded on one single M-line (at a depth of 10% of the plate thickness) was further processed with a Tukey window (with cosine fraction $r = 0.2$) to reduce windowing-related artefacts after Fourier transformation. The data were then converted to the f - k domain by means of a 2D fast Fourier transform, where the areas of maximum amplitude correspond to the dispersion curves. To reduce clutter, an amplitude mask was applied to the f - k data, filtering out amplitudes below 20% of the maximum. Only data for frequencies up to 600 Hz was considered during the analysis, to guarantee correct sampling of every wavelength included.

Only for the validation step, nine M-lines were drawn at depths from 10% to 50% of the thickness of the plate, with 5% increments, to enable a comparison with the experiments. The propagation measured on the nine M-lines were

then split in left- and right-halves, and the difference between left- and right-speeds at all depths was computed and averaged.

F. Numerical dispersion curve analysis and error map reconstruction

While space-time domain analysis based on Eq. (1) is still common in cardiac SWE studies, a more appropriate and theoretically sound approach to extract stiffness from wave propagation measurements is to analyse dispersion curves. The approach used to analyse $f-k$ domain data is summarised in Fig. 3. For each of the simulated waves, the data were extracted following the method described in Sec. IIE (panels 1–3 in Fig. 3). The extracted curve was then compared to a theoretical A0 curve with a specific bulk shear speed and thickness (panel 4 in Fig. 3). A root mean squared (RMS) percentage difference (PD) error function was introduced to quantify the comparison,

$$Err = \sqrt{\sum_i^N \frac{(100(K_i - K_i^T)/K_i^T)^2}{N}}, \quad (3)$$

where Err is the RMS-PD error, k_i is the wavenumber of the extracted curve at the i th frequency, k_i^T is the wavenumber of the chosen theoretical curve at the same frequency, and the sum runs over all N frequencies at which the curve was extracted. This comparison was repeated for all the theoretical curves within the parameter space (panel 5 in Fig. 3),

which comprised bulk shear speeds between 0.5 and 3.0 m/s (with a resolution of 0.001 m/s) and thicknesses between 2 mm and 10 mm (with a resolution of 0.1 mm). Plotting the RMS-PD value of each comparison in the same figure results in a 2D RMS-PD map (panel 6 in Fig. 3). The theoretical A0 curve that best fits the simulated one can then be identified as the minimum in the RMS-PD map. At the same time, the map shows how much the error grows when moving in the parameter space, and allows one to fix one parameter (e.g., thickness) and identify which value of the other one generates the lowest RMS-PD.

The shear speeds extracted from the $x-t$ data and from the best fitting curves in the $f-k$ domain were converted into values of the shear modulus G through Eq. (1), which is commonly used in most cardiac SWE studies. However, this equation only holds when c is the bulk shear speed. It should be kept in mind, therefore, that the speed derived from the $x-t$ data does not represent the bulk speed, since dispersion is occurring. At the same time, the $f-k$ analysis extracts the bulk shear speed for a flat plate, which is used as an approximation for the bulk shear speed in tapered plates in this study. To study how to minimize the impact of this approximation, different values of constant thickness were considered when extracting the speed from the RMS-PD maps: the extremal thicknesses of the plate (9 and 3 mm), the arithmetic mean of the thickness, and its harmonic mean. It can be shown that, at low frequencies, an A0 wave propagates across a tapered plate in approximately the same time it would take it to propagate across a plate of constant

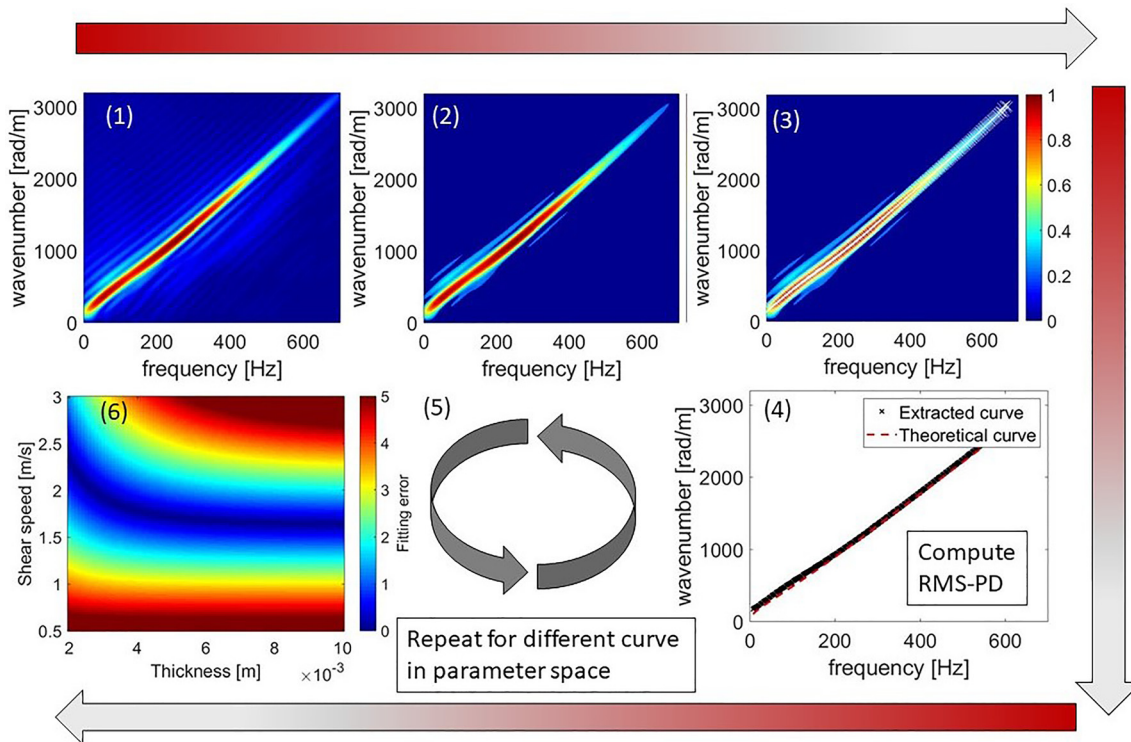


FIG. 3. (Color online) Procedure to reconstruct RMS-PD maps. (1) Retrieve $f-k$ data, (2) mask out 20% lowest amplitudes, (3) identify coordinates of maximal amplitude at every frequency, (4) compare with a theoretical A0 curve corresponding to one point in the parameter space and compute its RMS-PD, (5) repeat for all points in the parameter space, (6) make RMS-PD map for all parameters.

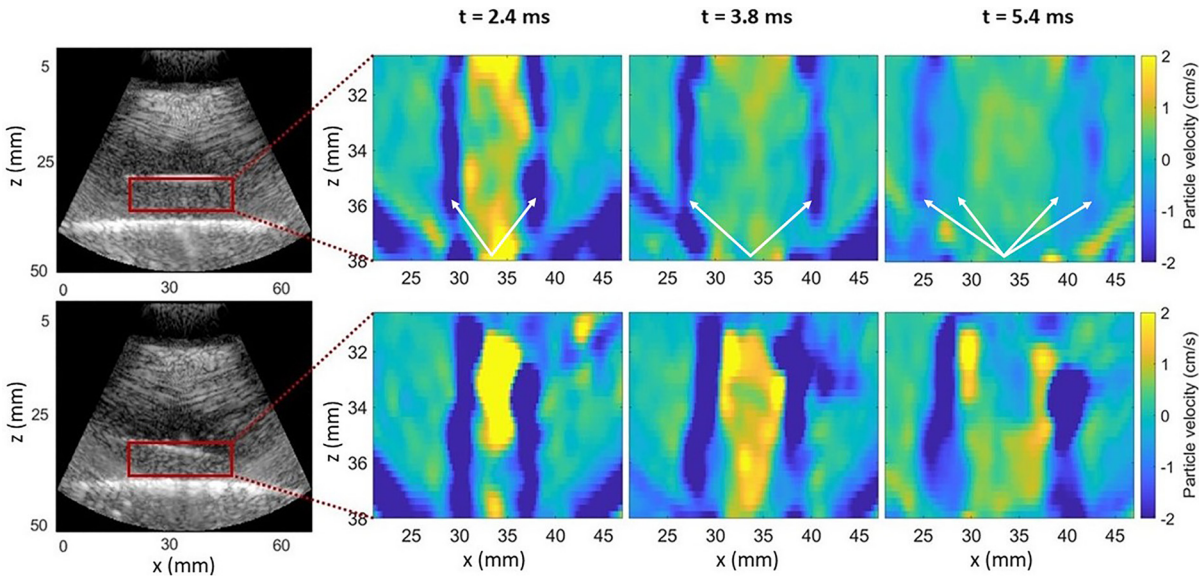


FIG. 4. (Color online) Snapshots of experimental wave propagation recorded in the flat (above) and tapered (below) sections of the PVA phantom, and B-mode view of the two sections (rightmost column). The ARF push was applied at $t = 0.0$ ms and was centered at $x = 34$ mm. The white arrows point at the propagation fronts. The colors in the propagation snapshots represent particle velocity in the z -direction.

thickness equal to the harmonic mean of the tapered thickness; at higher frequencies, the same result holds true for the arithmetic mean of the tapered thickness.

G. Effects of different IVS shapes

Since the real IVS can present a variety of different shapes, we simulated another tapered plate with the same material properties as before, the same total amount of tapering (i.e., a thickness variation between 9 and 3 mm), but a different shape, specifically a convex one (see Fig. 2). This model, in combination with the linearly tapered plate, allowed us to investigate whether the effects of tapering depend on how the thickness varies over space or rather just on the total thickness variation. For the purpose of this

comparison, the M-lines in the two tapered plates were drawn along their entire modelled length to ensure the same initial and final plate thickness along the M-line.

III. RESULTS

In this section we will first present the results of the experiments on a tapered phantom (Figs. 4 and 5), showing that waves propagate differently when they travel towards the thin or the thick ends of the plate. Then we show numerical results that allow a comparison of the simulations with theory and with the experiments (Figs. 6 and 7), for validation purposes. All subsequent results (Figs. 8 and 9, Tables I and II) are produced by simulations to investigate in more

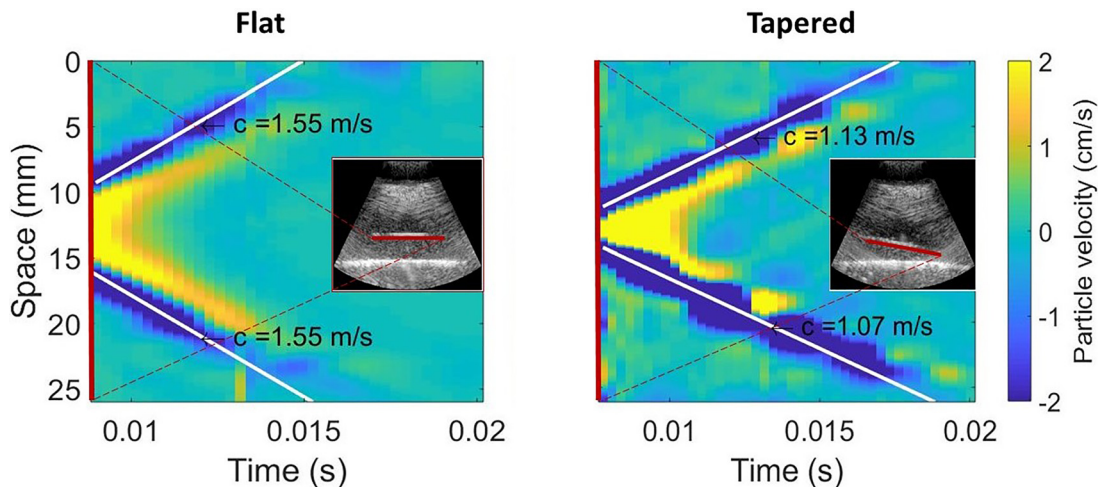


FIG. 5. (Color online) Experimental wave propagation recorded in the flat section (left) and tapered section (right) of a PVA phantom. The m-line (in red) was placed at about 1 mm of depth with respect to the top surface of the phantom (red line in the B-mode panels), centred with respect to the lateral coordinate of the focus of the ARF push beam. The propagation speed of the two wave branches is comparable in the flat section, whereas it decreases with thickness in the tapered part of the phantom. Colors represent particle velocity in the z -direction.

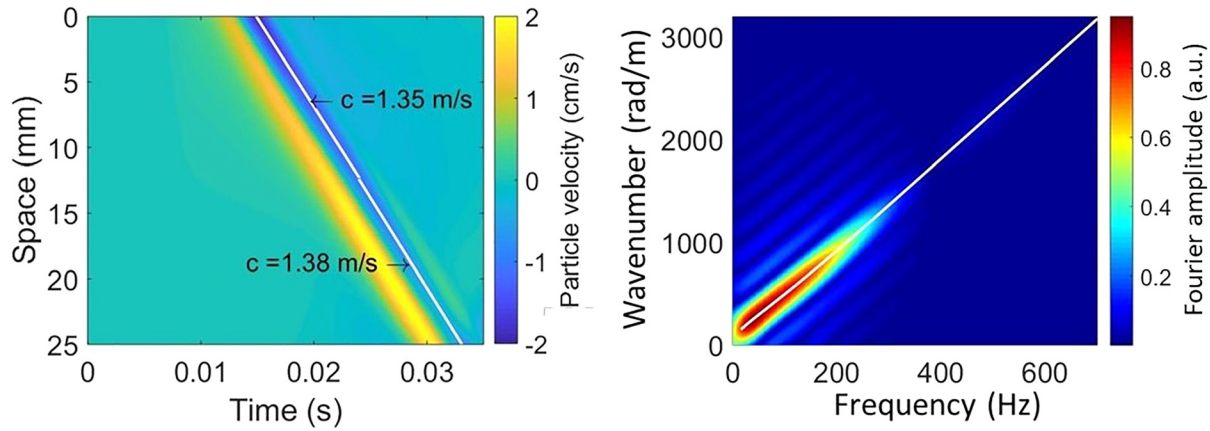


FIG. 6. (Color online) Simulated ARF wave propagation obtained along a 2.5 cm long m-line in a 4 cm long, 9 mm thick flat plate, at a depth of 0.9 mm. On the left, the wave is represented in the $x-t$ domain: the colour scheme represents particle velocity and the white lines show a Radon sum estimation of the trajectory of the wave. On the right, the wave is represented in the $f-k$ domain, with the white line representing the theoretical A0 dispersion curve for a plate surrounded by water with the same geometry and medium properties. The colour scheme represents the magnitude of the Fourier-transformed velocity recorded along the M-line.

detail the effects of tapering on the propagation of Lamb waves.

A. Experiments

Experiments were conducted on a PVA phantom to assess whether there are measurable differences in the propagation of a wave along flat and tapered sections of a plate. Figure 4 show snapshots of the propagating wave in two sections of the phantom (the upper panels depict the flat part of the phantom, whereas the lower panels illustrate the tapered part of the phantom). Three key features can be

observed in the propagation patterns. First, the waves propagating in the tapered section attenuate less rapidly than the one in the flat section. Second, the wave traveling in the flat section develops, during propagation, a split in left and right wavefronts at depths greater than approximately 20% of the thickness; this feature has already been reported in literature and is probably associated with the presence of the A1 mode besides the A0 mode.^{26,43} Third, close to the top surface in the flat section, the split is not present and the attenuation appears to be weaker.

In Fig. 5, the two panels show the experimental wave propagation measured along a single M-line at a depth of

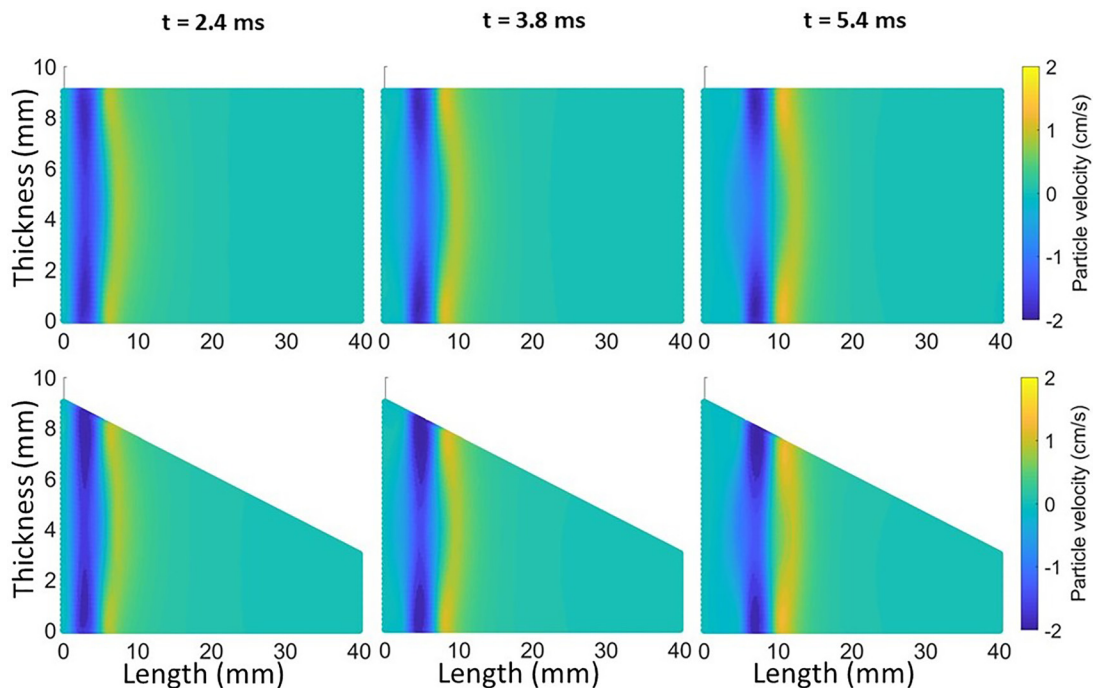


FIG. 7. (Color online) Snapshots of the propagation of a simulated ARF wave in a 4 cm long, 9 mm thick flat plate (top) and 9 to 3 mm tapered plate (bottom), both submerged in water.

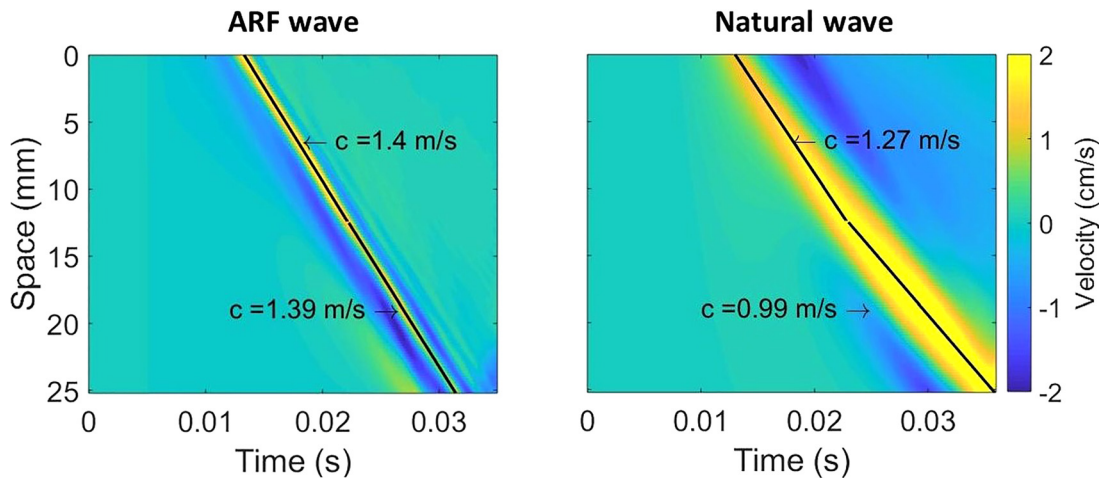


FIG. 8. (Color online) Space-time propagation of ARF waves (left) and naturally generated waves (right) in a plate with linear tapering between 9 and 3 mm. The black lines show the Radon sum estimation of the wave trajectories, considering the first and the second half of the travel path separately.

about 10% of the plate thickness in the flat (left panel) and tapered (right panel) sections. In the flat section, both branches of the wave propagate with a speed of 1.55 m/s, whereas, in the tapered section, the two branches have different speeds: the branch propagating towards the thicker end travels at 1.13 m/s, while the other branch travels at 1.07 m/s. Analysing nine M-lines across the phantom thickness in the flat section, the average speed difference (with standard deviation) between left and right branch is 0.01 ± 0.04 m/s, which is negligible in magnitude with respect to the standard deviation. In contrast, performing the same analysis on data measured in the tapered section, and taking into account nine M-lines again, the average difference between left and right speeds is 0.16 ± 0.07 m/s, which is considerably larger than its standard deviation. We can conclude that tapering causes the wave to decelerate during propagation towards the thinner end. An example wave propagation pattern of the top M-line in the tapered plate is

shown in the right panel of Fig. 5, where the wave branches traveling towards the thick and thin ends have speeds of 1.13 and 1.07 m/s, respectively.

B. Simulations

1. Validation

The two panels in Fig. 6 present the propagation of simulated ARF waves obtained in the flat plate along a 2.5 cm long M-line placed at a depth of 0.9 mm in $x-t$ and $f-k$ domains (left and right panels, respectively). In the $x-t$ domain plots, the superimposed white lines show the propagation trajectory estimated by the Radon sum algorithm, corresponding to speeds of 1.35 and 1.38 m/s. The white line in the $f-k$ domain plots represent the theoretical A0 mode, computed for a flat 9 mm thick fluid-loaded plate. The gradient of this line indicates a propagation speed that ranges between 0.5 m/s for $f=10$ Hz and 1.4 m/s for

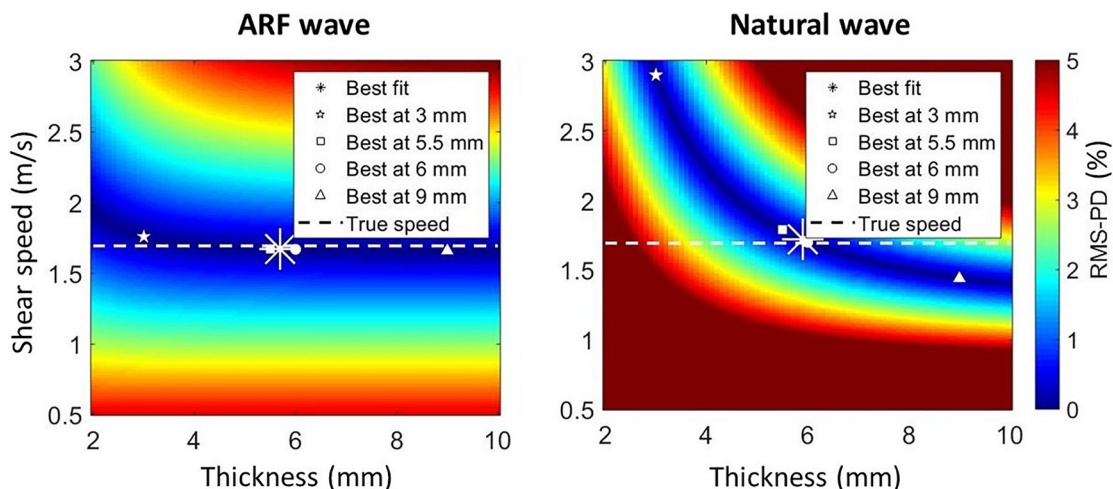


FIG. 9. (Color online) RMS-PD maps for the ARF (left) and natural (right) waves in a plate with linear tapering between 9 and 3 mm. The white star shows the coordinates of the curve with minimal RMS-PD; the white filled polygons indicate the coordinates of the best fitting curves at a fixed thickness of 3 mm (star), 5.5 mm (square), 6 mm (circle), and 9 mm (triangle). The dashed line shows the true value of bulk shear speed in the simulated material. The colour scheme represents the amplitude of the fitting error, i.e., the RMS-PD value.

TABLE I. Percentage error in the estimation of modelled G (3 kPa), based on the bulk shear speed extracted from $x-t$ data and by fitting the simulated A0 of a linearly tapering plate. For the A0 fitting, theoretical curves were considered corresponding to flat plates with different constant values of thickness (h). 6 mm is the arithmetic mean of the thickness of the plate, 5.5 mm is its harmonic mean. The best fitting curve for the ARF data corresponds to a thickness of 5.7 mm, while for the natural wave it corresponds to a thickness of 5.9 mm. In the $x-t$ domain column, two percentages are given, representing the values computed for the left and right halves of the M-lines. The positive sign indicates overestimation, the negative sign underestimation.

| Error in shear modulus estimation | | | | | | |
|-----------------------------------|-----------------------|-----------------------|------------|--------------|------------|----------|
| Excitation type | $x-t$ domain analysis | $f-k$ domain analysis | | | | Best fit |
| | | $h = 9$ mm | $h = 6$ mm | $h = 5.5$ mm | $h = 3$ mm | |
| ARF | -34.7% (left) | -4.0% | -2.9% | -2.8% | +7.9% | -2.9% |
| | -35.6% (right) | | | | | |
| Natural | -46.2% (left) | -27.8% | +0.7% | +11.6% | +192.9% | +3.0% |
| | -67.3% (right) | | | | | |

$f = 600$ Hz. In particular, the good match between the theoretical A0 curve and the curve extracted from the simulated wave (RMS-PD of 0.12%) confirms that the numerical settings employed in our model are adequate for reliable simulations.

To compare numerical and experimental results, the speeds were further analysed separately for the left and right halves of nine M-lines at depths between 0.9 and 4.5 mm. The speed difference between left and right branches was averaged over these nine M-lines, yielding an average difference of 0.01 ± 0.02 m/s, confirming that the simulated wave does not undergo variations of speed in a plate with constant thickness. Moreover, performing the same analysis for the simulated tapered plate, the average propagation speed difference between left and right halves was found to be 0.10 ± 0.05 m/s, confirming that the simulations capture correctly the deceleration introduced by tapering.

Figure 7 shows snapshots of the propagation of the simulated ARF waves propagating in a flat 9 mm thick plate (top) and a plate with thickness tapering between 9 and 3 mm (bottom). Comparing qualitatively the experimental and simulated propagation snapshots in the flat plate, we can notice that the three features identified in the experimental data are also present, to some extent, in the simulations: the wave appears to attenuate less in the tapered plate and closer to the surfaces, and the wavefront in the central section of the simulated plate presents a distortion similar to the

wavefront splitting observed in the experiments. In the simulated data, however, a wavefront with positive amplitude also appears in front of the original wave, which was not observed in the experimental data and which appears to increase in amplitude during propagation.

2. ARF versus natural waves in a linearly tapered plate

Due to their different frequency contents, natural and ARF-generated waves can be expected to be affected differently by the tapering of the plate. To investigate this, Fig. 8 shows two simulated waves (one ARF-based and one natural) in the $x-t$ domain, tracked on an M-line at a depth of 10% of the plate thickness. The black lines indicate the Radon sum extracted trajectory. While the ARF-induced wave propagates with an essentially constant speed along the entire length of the M-line (1.40 m/s in the first half, 1.39 m/s in the second half), it is clear that the $x-t$ trajectory of the natural wave is curved: two lines with different inclinations fit the first and the second halves of the trajectory, resulting in speeds of 1.27 and 0.99 m/s, respectively. This result is in agreement with theoretical expectations, since the phase speed of the A0 mode is lower at lower frequency-thickness products.

Figure 9 displays the error maps corresponding to an ARF wave (left panel) and a natural wave (right panel), computed as described in Fig. 3. As can be observed in

TABLE II. Percentage error in the estimation of modelled G (3 kPa), based on the bulk shear speed extracted from $x-t$ data and by fitting the simulated A0 of a convex tapered plate. For the A0 fitting, theoretical curves were considered corresponding to flat plates with different constant values of thickness (h). 7.7 mm is the arithmetic mean of the thickness of the plate, 6.9 mm is its harmonic mean. The lowest RMS-PD curve at a thickness of 3 mm, for the natural wave, corresponded to a bulk shear speed greater than 3 m/s, outside the boundaries of the parameter space considered. The best fitting curve for the ARF data corresponds to a thickness of 6.7 mm, while for the natural wave it corresponds to a thickness of 7.3 mm. In the $x-t$ domain column, two values of percentages are given, representing the values computed for the left and right halves of the M-lines.

| Error in shear modulus estimation | | | | | | | |
|-----------------------------------|-----------------------|-----------------------|--------------|--------------|------------|----------|------------|
| Excitation type | $x-t$ domain analysis | $f-k$ domain analysis | | | | Best fit | |
| | | $h = 9$ mm | $h = 7.7$ mm | $h = 6.9$ mm | $h = 6$ mm | | $h = 3$ mm |
| ARF | -25.7% (left) | -2.9% | -1.7% | -1.7% | -1.7% | +10.4% | -1.7% |
| | -27.7% (right) | | | | | | |
| Natural | -35.6% (left) | -5.2% | +7.9% | +19.2% | +39.3% | >+213.5% | +12.9% |
| | -44.7% (right) | | | | | | |

Fig. 9, the RMS-PD maps for ARF waves and naturally generated waves are quite different, with the natural waves showing a greater sensitivity to the thickness parameter, as can be expected: at the higher frequencies typical of ARF waves, the A0 curve is flat and insensitive to thickness variations, whereas at the low frequencies of natural waves the dispersion curve is slanted and the phase speed varies considerably with the thickness. Indeed, with natural waves, depending on which thickness value is used as input to identify the best-fitting bulk shear speed, the value of the latter can vary greatly. Moreover, it can be seen for both waves that neglecting the tapering and assuming a thickness of 9 mm results in a higher RMS-PD than, for instance, assuming a thickness of 6 mm (corresponding to the average thickness of the plate). Underestimating the thickness also leads to higher RMS-PD, as well as higher estimated speed for both waves.

To obtain Table I, first the curves with lowest RMS-PD were identified for different fixed values of plate thickness. Then, the shear modulus G was computed via Eq. (1) using the corresponding bulk shear speed. Finally, the value of G thus obtained was compared with the input value of the simulation. As can be seen from this table, assuming an unchanged equatorial thickness of 9 mm leads to underestimation of G , resulting in especially large errors when analysing natural waves (4% underestimation for ARF waves, 27% underestimation for natural waves). Furthermore, as was already visible from the error distribution portrayed in Fig. 9, underestimating the thickness of the plate (e.g., assuming a thickness of 3 mm) can lead to overestimations of G for both wave types, especially severe in the case of natural waves. Finally, Table I reports the results of assuming a constant thickness corresponding to either the arithmetic mean (6 mm) or harmonic mean (5.5 mm) of the plate thickness.

3. ARF versus natural waves in a convex tapered plate

The RMS-PD maps for the curves extracted for the convex plate were used to produce Table II, from which it can be seen that the shape plays a role on how the wave is affected by the tapering. The difference between the G estimated for the left and right halves of the M-line in $x-t$ domain is smaller in the convex plate, meaning that the wave decelerates less during propagation. Moreover, we note that fitting the A0 mode assuming a thickness of 6 mm, a viable solution in the linearly tapered plate, now can result in severe overestimation of the shear modulus, especially for the natural waves. Smaller deviations from the actual implemented shear modulus are obtained by setting the thickness to either 6.9 or 7.7 mm, the harmonic mean and arithmetic mean of the thickness of the convex slab, respectively. Moreover, the bulk shear speed of the curve with lowest RMS-PD for a thickness of 3 mm was greater than 3 m/s, outside the boundaries of the parameter space considered to build the RMS-PD maps (as indicated by $> +213.5\%$ in Table II).

IV. DISCUSSION

A. Effects of tapering on SWE measurements

In this work, we have investigated how cardiac SWE measurements of material properties may be affected by the tapering of the IVS. The effects of tapering have already been investigated^{32–34} in the non-medical field for waves with relatively high frequency contents (e.g., from 0.7 to 3.3 MHz³³) where multiple higher order symmetric and anti-symmetric modes are present. These studies showed that such higher modes, which only appear above well-defined values of the frequency-thickness product, can be reflected or converted into lower order modes when the thickness decreased sufficiently. However, the waves analysed in cardiac SWE have a relatively low frequency content (typically within 1000 Hz^{19,22,27,28}) and are therefore characterized mainly by the zero-order modes and the first-order modes: the former are present at all frequency-thickness products, and, for the latter, cardiac thickness reductions are not large enough for mode conversion. Therefore, the effects described in literature would be hardly observed in the context of cardiac SWE.

Nevertheless, the thickness variation of the IVS can introduce effects that are relevant for cardiac SWE, especially for natural waves, as these are characterised by a stronger dispersion due to their lower frequency-thickness product. Both experiments and simulations showed that the wave speed extracted in the $x-t$ domain can vary considerably along the plate with decreasing thickness, especially for waves with lower frequency contents (a $\sim 10\%$ speed decrease between the two branches in the experimental ARF data, and $\sim 29\%$ speed variation in the simulations of the natural waves, as shown in Figs. 5 and 8). As shown in Table I, shear moduli obtained from the wave speed in the $x-t$ domain severely underestimate the input value of $G = 3$ kPa for both ARF ($G = 2$ kPa) and natural waves ($G = 1.7$ kPa and $G = 1.0$ kPa for left and right wave, respectively) simulations. For comparison, the values of G extracted from $x-t$ data in the simulated flat plate are $G = 2.1$ kPa for the ARF wave and $G_{NAT} = 1.8$ kPa for the natural wave. From these results, we conclude that thickness variations exacerbate the error that is already introduced by analysing waves in the IVS in the $x-t$ domain, with an additional decrease in stiffness estimation of 3% for ARF waves and even 27% for natural waves.

Interestingly, as we mentioned in the introduction, Keijzer *et al.*⁸ have recently reported that by using $x-t$ domain analysis, a variability of up to approximately 40% in the speed of naturally induced aortic valve closure (AVC) waves can be found between different studies, with variations on the order of 20% between measurements within each study. As shown in Fig. 8, even the same measurement of natural wave propagation in a tapered plate could yield speeds that vary by 30% from each other using the time domain analysis. It is also reasonable to assume that different hearts would present slightly different shapes, even among healthy volunteers, potentially increasing further the

difference between measurements, as suggested by Tables I and II. Based on our results, therefore, we suggest that geometry of the IVS plays a role in the variability of the speeds being reported.

In principle, analysing the propagation data in the f - k domain should provide a more robust method of deriving G , since fitting the dispersion curves allows one to determine the value of the bulk shear speed, which is directly related to the shear modulus.^{4,11,19,20,26,27} However, as is apparent from Tables I and II, knowledge on the specific shape of the observed IVS is necessary in order to perform the fit correctly. Our results show, in fact, that neglecting the thickness variations can lead to considerable overestimation and underestimation of the shear modulus, and that a significant role is played by the exact shape of the plate, as opposed to the overall thickness reduction. The relevance of accounting for the correct thickness of the plate was also observed, for plates of constant thickness, by Maksuti *et al.*,⁴⁴ who showed the error introduced by inaccurate thickness assumptions in arterial SWE.

The RMS-PD maps demonstrate a sub-region of the parameter space corresponding to dispersion curves with RMS-PD < 1% (see Fig. 9). Within this region, especially for natural waves, small variations on the thickness axis can lead to big variations of the bulk shear speed with minimum RMS-PD, while still generating very similar dispersion curves. When using the global minimum of the RMS-PD map, even small errors in the reconstruction of the experimental or simulated dispersion curve could then lead to the wrong parameters. For this reason, it is our opinion that the global minimum of the two-parameters space should be avoided for reconstructing material properties of the IVS; rather, *a priori* knowledge of one of the two parameters (e.g., the thickness) should be used as input to identify the other.

In terms of clinical applications, our results confirm that determining the shear modulus from SWE measurements is more accurately done by analysing dispersion curves in the f - k domain, rather than employing Eq. (1) on the wave speed directly obtained from the x - t data, as had already been suggested in literature.^{26,44} The thickness of the IVS can be measured for instance from B-mode images and used as input in the fitting procedure employed for the dispersion curves. In particular, to obtain more reliable results when there are thickness variations over the M-line, the thickness at each point should be measured and combined to compute some mean value, as opposed to averaging the total thickness variation. If precise information about the thickness is not available, our results suggest that overestimating the thickness leads to smaller errors than underestimating it, which is due to the shape of the A0 dispersion curve and is consistent with earlier observations.⁴⁴

A major challenge to this application, however, lies in the reconstruction of the experimental dispersion curve: resolution in the f - k domain depends on the size (in space and time) of the acquisition of the x - t signal, which is typically limited in cardiac applications to a few milliseconds over a

couple of centimetres (determined by acquired field-of-view for the IVS).^{22,26} The resulting resolution in the f - k domain is thus low and potentially compounded to imaging artefacts and gross motion of the heart, which could lead to inaccuracies in the reconstruction of the dispersion curve, therefore affecting the result of the fit. This issue can be especially significant for natural waves, due to their longer wavelengths. In fact, even in the relatively simple setup considered for our phantom experiments, the resolution of the f - k data were too low to extract the dispersion curve. Accounting for the effects of plate geometry directly in the analysis of data in the x - t domain may circumvent the challenging resolution of the transformed domain; further research will be necessary to investigate and develop such an approach.

Finally, it is worth noting that the results found for the A0 curve are relevant for the S0 mode as well: in the frequency range typical of natural waves, the S0 mode shows a dispersion comparable to (and even slightly larger than) the one of A0, albeit opposite in sign. A visual comparison of A0 and S0 in a (flat) plate submerged in water, for frequencies relevant to the present work, can be found in a recent work by Keijzer *et al.*⁴⁵

From a theoretical point of view, it is incorrect to talk about Lamb dispersion curves in plates of varying thickness, as these curves are defined for flat plates. Regardless, as a practical attempt to extract the shear modulus from wave measurements, it may still be useful to fit the known curves of a fluid-loaded flat plate to the f - k data. Performing the fit by using the average thickness of the plate, for example, yielded relatively accurate results for the linearly tapered plate; however, it did not show any advantage over using the maximal thickness for the fit performed for the convex plate. Moreover, while the harmonic mean could be expected to provide a better approximation (since a wave traveling in a flat plate of equivalent thickness propagates with the same average speed as one traveling in a tapered plate), it did not yield better results. This suggests that an average thickness can be a useful first approximation that should be improved upon.

B. Simulations versus experiments

The numerical settings of the simulations were validated by comparing the A0 curve of a simulated flat plate with the corresponding theoretical curve, showing a good correspondence between the two. Furthermore, the deceleration introduced by tapering observed in experiments is also present in the simulation data, confirming that our simulations can reliably reproduce wave physics also in the case of a tapered plate. To some extent, the main features of the propagation patterns in x - t domain of the experimental data are visible also in the simulations. However, in the simulations of the flat plate the splitting of the wavefront is not as clearly visible as in the experiments. Moreover, in the simulations, a positive wavefront appears during propagation, while this is not observed in the experimental data.

The imperfect match between the simulated and experimental patterns could have several causes: for one, the wave source employed in our numerical study was meant to simulate the frequency content of the experimental wave, but the space-time distribution of the simulated source in the plate was kept much simpler. Additionally, the modelled plate is perfectly elastic, homogeneous and isotropic, whereas the plate used for the experiments could contain imperfections due to fabrication, which could in turn affect the wave patterns.

Finally, the deceleration observed during the experiments appears to be larger in magnitude than that reported in Table I for the simulations. One likely cause for this discrepancy is that the stiffness of the phantom was higher than the one modelled numerically, as supported by the higher propagation speed along the flat section. As a consequence of the higher stiffness, the overall variation in the phase speed of the A0 mode is greater, since it plateaus at a higher magnitude for high frequencies, while it still approaches zero for vanishing frequency-thickness products. Moreover, the frequency band of our experimental signal contained lower frequencies than that of the ARF simulated signal considered in Table I (approximately 10–250 Hz for the experimental frequency band, 10–600 Hz for the simulations reported in the table). Due to the lower frequency content of the experiment, it is expected that the effects of the thickness variations would be greater and closer to those of the simulated natural wave.

C. Limitations

In order to model a realistic cardiac shape, the fabricated phantom resulted in a relatively wide and thin plate with density just slightly higher than that of water. When submerged, the phantom tended to float around and curl at the thin edges. To prevent these effects, 3D printed PLA supports were fabricated and placed underneath and on top of the plate at two opposite ends. While the supports were never included in the field of view of the probe during experiments, their presence and contacts with the plate may also have affected the wave propagation by changing the actual boundary conditions of the wave guide.

To show the effects of tapering on propagation in $x-t$ domain, we reported two values of speeds (corresponding to the first and second halves of the propagation). This approximation is useful to offer a clear, simple view of the effect of tapering, especially in the experimental data, where the resolution may not be high enough to discern local, small-magnitude variations. However, the propagation speed is a continuous function of space, since the tapering is, and the propagation trajectory is curved. By reporting only two values of constant speed, information on the precise variation of propagation speed over space is therefore lost.

Finally, to isolate the effects of tapering, several simplifications were made in our experimental and numerical models compared to actual cardiac settings: the IVS was modelled as a purely elastic, isotropic plate, whereas cardiac

tissue is known to show both viscoelastic and anisotropic behaviour, as well as inhomogeneities near the valves. In conjunction with the three-dimensional curvature of a real IVS, all these parameters would likely affect the trajectory, attenuation, and dispersion of the propagating waves. Such effects were beyond the scope of this study, but should be included in future work to produce a more realistic model for the interpretation of SWE measurements in terms of medium properties.

V. CONCLUSIONS

In conclusion, this work shows experimentally and numerically that the specific (variable) thickness of the IVS can affect the estimation of the shear modulus obtained by SWE, especially when low frequency waves, such as natural waves, are tracked. Experiments show a shear wave speed deceleration of 11% in a 4 cm long plate with thickness tapering down from 9 to 3 mm. The numerical results show that neglecting tapering in $f-k$ analyses can result in errors greater than 30% in shear modulus estimation, and that $x-t$ analyses based on Eq. (1) are even less accurate. Finally, the exact tapering curve of the plate, rather than its absolute thickness variation, determines these effects, and more accurate results can be obtained when the constant thickness value considered for the $f-k$ analysis equals the mean thickness of the plate.

ACKNOWLEDGMENTS

This work is part of the STW–Dutch Heart Foundation partnership program “Earlier recognition of cardiovascular diseases” with Project No. 14740, which is financed (in part) by The Netherlands Organization for Scientific Research (NWO).

- ¹J. E. Brandenburg, S. F. Eby, P. Song, H. Zhao, J. S. Brault, S. Chen, and K.-N. An, “Ultrasound elastography: The new frontier in direct measurement of muscle stiffness,” *Arch. Phys. Med. Rehab.* **95**(11), 2207–2219 (2014).
- ²L. C. Carlson, T. J. Hall, I. M. Rosado-Mendez, L. Mao, and H. Feltovich, “Quantitative assessment of cervical softening during pregnancy with shear wave elasticity imaging: An *in vivo* longitudinal study,” *Interf. Foc.* **9**(5), 20190030 (2019).
- ³G. Ferraioli, C. Tinelli, B. Dal Bello, M. Zicchetti, G. Filice, and C. Filice, “Accuracy of real-time shear wave elastography for assessing liver fibrosis in chronic hepatitis C: A pilot study,” *Hepatology* **56**(6), 2125–2133 (2012).
- ⁴C. Pislaru, M. Urban, I. Nenadic, and J. Greenleaf, “Shearwave dispersion ultrasound vibrometry applied to *in vivo* myocardium,” in *2009 Annual International Conference of the IEEE Engineering in Medicine and Biology Society*, IEEE (2009), pp. 2891–2894.
- ⁵C. Pislaru, M. W. Urban, S. V. Pislaru, R. R. Kinnick, and J. F. Greenleaf, “Viscoelastic properties of normal and infarcted myocardium measured by a multifrequency shear wave method: Comparison with pressure-segment length method,” *Ultrasound Med. Biol.* **40**(8), 1785–1795 (2014).
- ⁶M. Strachinaru, J. G. Bosch, B. M. van Dalen, L. van Gils, A. F. van der Steen, N. de Jong, M. L. Geleijnse, and H. J. Vos, “Cardiac shear wave elastography using a clinical ultrasound system,” *Ultrasound Med. Biol.* **43**, 1596–1606 (2017).
- ⁷M. Strachinaru, J. G. Bosch, L. van Gils, B. M. van Dalen, A. F. L. Schinkel, A. F. W. van der Steen, N. de Jong, M. Michels, H. J. Vos, and M. L. Geleijnse, “Naturally occurring shear waves in healthy volunteers

- and hypertrophic cardiomyopathy patients,” *Ultrasound Med. Biol.* **45**(00), 1977–1986 (2019).
- ⁸L. B. Keijzer, M. Strachinaru, D. J. Bowen, M. L. Geleijnse, A. F. van der Steen, J. G. Bosch, N. de Jong, and H. J. Vos, “Reproducibility of natural shear wave elastography measurements,” *Ultrasound Med. Biol.* **45**(12), 3172–3185 (2019).
- ⁹W. H. Gaasch, H. J. Levine, M. A. Quinones, and J. K. Alexander, “Left ventricular compliance: Mechanisms and clinical implications,” *Am. J. Cardiol.* **38**(5), 645–653 (1976).
- ¹⁰D. Westermann, M. Kasner, P. Steendijk, F. Spillmann, A. Riad, K. Weitmann, W. Hoffmann, W. Poller, M. Pauschinger, H.-P. Schultheiss, and C. Tschope, “Role of left ventricular stiffness in heart failure with normal ejection fraction,” *Circulation* **117**(16), 2051–2060 (2008).
- ¹¹H. Kanai, “Propagation of spontaneously actuated pulsive vibration in human heart wall and in vivo viscoelasticity estimation,” *IEEE Trans. Ultrason. Ferroelectr. Freq. Control* **52**(11), 1931–1942 (2005).
- ¹²C. Pislaru, P. A. Pellikka, and S. V. Pislaru, “Wave propagation of myocardial stretch: Correlation with myocardial stiffness,” *Basic Res. Cardiol.* **109**(6), 438–450 (2014).
- ¹³H. J. Vos, B. M. van Dalen, I. Heinonen, J. G. Bosch, O. Sorop, D. J. Duncker, A. F. W. van der Steen, and N. de Jong, “Cardiac shear wave velocity detection in the porcine heart,” *Ultrasound Med. Biol.* **43**(4), 753–764 (2017).
- ¹⁴P. Santos, A. M. Petrescu, J. Pedrosa, M. Orlowska, V. Komini, J.-U. Voigt, and J. D’hooge, “Natural shear wave imaging in the human heart: Normal values, feasibility, and reproducibility,” *IEEE Trans. Ultrason. Ferroelectr. Freq. Control* **66**(3), 442–452 (2019).
- ¹⁵M. Couade, M. Pernot, E. Messas, A. Bel, M. Ba, A. Hagege, M. Fink, and M. Tanter, “In vivo quantitative mapping of myocardial stiffening and transmural anisotropy during the cardiac cycle,” *IEEE Trans. Medical Imaging* **30**(2), 295–305 (2011).
- ¹⁶M. Pernot, W.-N. Lee, A. Bel, P. Mateo, M. Couade, M. Tanter, B. Crozatier, and E. Messas, “Shear wave imaging of passive diastolic myocardial stiffness,” *JACC: Cardiovasc. Imag.* **9**(9), 1023–1030 (2016).
- ¹⁷P. Song, X. Bi, D. C. Mellema, A. Manduca, M. W. Urban, J. F. Greenleaf, and S. Chen, “Quantitative assessment of left ventricular diastolic stiffness using cardiac shear wave elastography,” *J. Ultrasound Med.* **35**(7), 1419–1427 (2016).
- ¹⁸O. Villemain, M. Correia, E. Mousseaux, J. Baranger, S. Zarka, I. Podetti, G. Soulat, T. Damy, A. Hagège, M. Tanter, M. Pernot, and E. Messas, “Myocardial stiffness evaluation using noninvasive shear wave imaging in healthy and hypertrophic cardiomyopathic adults,” *JACC: Cardiovasc. Imag.* **12**(7), 1135–1145 (2019).
- ¹⁹H. Kanai, “2H-5 Regional Differences in Phase Velocity of Pulsive Wave Propagating Along the Heart Wall,” in *2006 IEEE Ultrasonics Symposium*, IEEE (2006), pp. 760–763.
- ²⁰I. Z. Nenadic, M. W. Urban, S. A. Mitchell, and J. F. Greenleaf, “Lamb wave dispersion ultrasound vibrometry (LDUV) method for quantifying mechanical properties of viscoelastic solids,” *Phys. Med. Biol.* **56**(7), 2245–2264 (2011).
- ²¹N. Bekki and S. A. Shintani, “Simple dispersion equation based on Lamb-Wave model for propagating pulsive waves in human heart wall,” *J. Phys. Soc. Jpn.* **84**(12), 124802 (2015).
- ²²H. J. Vos, B. M. van Dalen, J. G. Bosch, A. F. van der Steen, and N. de Jong, “Myocardial passive shear wave detection,” in *2015 IEEE International Ultrasonics Symposium (IUS)*, IEEE (2015), pp. 1–4.
- ²³J. Rose, *Ultrasonic Guided Waves Solid Media* (Cambridge University Press, Cambridge, 2014).
- ²⁴M. Bernal, I. Nenadic, M. W. Urban, and J. F. Greenleaf, “Material property estimation for tubes and arteries using ultrasound radiation force and analysis of propagating modes,” *J. Acoust. Soc. Am.* **129**(3), 1344–1354 (2011).
- ²⁵B. Brekke, L. C. Nilsen, J. Lund, H. Torp, T. Bjastad, B. H. Amundsen, A. Stoylen, and S. A. Aase, “Ultra-high frame rate tissue doppler imaging,” *Ultrasound Med. Biol.* **40**(1), 222–231 (2014).
- ²⁶A. Caenen, M. Pernot, D. A. Shcherbakova, L. Mertens, M. Kersemans, P. Segers, and A. Swillens, “Investigating shear wave physics in a generic pediatric left ventricular model via in vitro experiments and finite element simulations,” *IEEE Trans. Ultrason. Ferroelectr. Freq. Control* **64**(2), 349–361 (2017).
- ²⁷I. Z. Nenadic, M. W. Urban, C. Pislaru, D. Escobar, L. Vasconcelos, and J. F. Greenleaf, “In vivo open- and closed-chest measurements of left-ventricular myocardial viscoelasticity using Lamb wave dispersion ultrasound vibrometry (LDUV): A feasibility study,” *Biomed. Phys. Eng. Exp.* **4**(4), 047001 (2018).
- ²⁸E. Maksuti, E. Widman, D. Larsson, M. W. Urban, M. Larsson, and A. Bjällmark, “Arterial stiffness estimation by shear wave elastography: Validation in phantoms with mechanical testing,” *Ultrasound Med. Biol.* **42**(1), 308–321 (2016).
- ²⁹P. H. M. Bovendeerd, J. Rijcken, D. H. Van Campen, A. J. G. Schoofs, K. Nicolay, and T. Arts, “Optimization of left ventricular muscle fiber orientation,” in *IUTAM Symposium on Synthesis in Bio Solid Mechanics. Solid Mechanics and its Applications*, edited by P. Pedersen and M. P. Bendsøe (Springer, Dordrecht, 1999), pp. 285–296.
- ³⁰P. T. Lee, M. R. Dweck, S. Prasher, A. Shah, S. E. Humphries, D. J. Pennell, H. E. Montgomery, and J. R. Payne, “Left ventricular wall thickness and the presence of asymmetric hypertrophy in healthy young army recruits: Data from the LARGE heart study,” *Circ.: Cardiovasc. Imag.* **6**(2), 262–267 (2013).
- ³¹A. J. Baxi, C. S. Restrepo, D. Vargas, A. Marmol-Velez, D. Ocazonez, and H. Murillo, “Hypertrophic cardiomyopathy from A to Z: Genetics, pathophysiology, imaging, and management,” *Radiographics* **36**(2), 335–357 (2016).
- ³²Y. Cho, “Estimation of ultrasonic guided wave mode conversion in a plate with thickness variation,” *IEEE Trans. Ultrason. Ferroelectr. Freq. Control* **47**(3), 591–603 (2000).
- ³³M.-C. El-Kettani, F. Luppé, and A. Guillet, “Guided waves in a plate with linearly varying thickness: Experimental and numerical results,” *Ultrasonics* **42**(1-9), 807–812 (2004).
- ³⁴M. E.-C. El-Kettani, M. V. Predoi, and P. Marical, “5K-6 experimental and numerical studies on Lamb waves conversion in a waveguide with Gaussian section variation,” in *2006 IEEE Ultrasonics Symposium*, IEEE (2006), pp. 1185–1188.
- ³⁵L. Keijzer, A. Sabbadini, J. G. Bosch, M. D. Verweij, A. F. Van Der Steen, N. D. Jong, and H. J. Vos, “Diffuse shear wave elastography in a thin plate phantom,” in *IEEE International Ultrasonics Symposium, IUS* (2017).
- ³⁶C. Kasai, K. Namekawa, A. Koyano, and R. Omoto, “Real-time two-dimensional blood flow imaging using an autocorrelation technique,” *IEEE Trans. Sonics Ultrason.* **32**(3), 458–464 (1985).
- ³⁷N. C. Rouze, M. H. Wang, M. L. Palmeri, and K. R. Nightingale, “Robust estimation of time-of-flight shear wave speed using a Radon sum transformation,” *Proceedings—IEEE Ultrasonics Symposium* **57**(12), 21–24 (2010).
- ³⁸M. L. Palmeri, A. C. Sharma, R. R. Bouchard, R. W. Nightingale, and K. R. Nightingale, “A finite-element method model of soft tissue response to impulsive acoustic radiation force,” *IEEE Trans. Ultrason. Ferroelectr. Freq. Control* **52**(10), 1699–1712 (2005).
- ³⁹I. Z. Nenadic, B. Qiang, M. W. Urban, L. H. De Araujo Vasconcelo, A. Nabavizadeh, A. Alizad, J. F. Greenleaf, and M. Fatemi, “Ultrasound bladder vibrometry method for measuring viscoelasticity of the bladder wall,” *Phys. Med. Biol.* **58**(8), 2675–2695 (2013).
- ⁴⁰A. Caenen, D. Shcherbakova, B. Verheghe, C. Papadacci, M. Pernot, P. Segers, and A. Swillens, “A versatile and experimentally validated finite element model to assess the accuracy of shear wave elastography in a bounded viscoelastic medium,” *IEEE Trans. Ultrason. Ferroelectr. Freq. Control* **62**(3), 439–450 (2015).
- ⁴¹M. L. Palmeri, B. Qiang, S. Chen, and M. W. Urban, “Guidelines for finite-element modeling of acoustic radiation force-induced shear wave propagation in tissue-mimicking media,” *IEEE Trans. Ultrason. Ferroelectr. Freq. Control* **64**(1), 78–92 (2017).
- ⁴²S. L. Lipman, N. C. Rouze, M. L. Palmeri, and K. R. Nightingale, “Impact of acoustic radiation force excitation geometry on shear wave dispersion and attenuation estimates,” *Ultrasound Med. Biol.* **44**(4), 897–908 (2018).
- ⁴³A. Sabbadini, A. Caenen, H. J. Vos, N. D. Jong, and M. D. Verweij, “Numerical model of Lamb wave propagation in the tapered septal wall of the heart,” in *Proceedings of Meetings on Acoustics* (2019), Vol. 39.
- ⁴⁴E. Maksuti, F. Bini, S. Fiorentini, G. Blasi, M. W. Urban, F. Marinuzzi, and M. Larsson, “Influence of wall thickness and diameter on arterial shear wave elastography: A phantom and finite element study,” *Phys. Med. Biol.* **62**(7), 2694–2718 (2017).
- ⁴⁵L. B. Keijzer, M. Strachinaru, D. J. Bowen, A. Caenen, A. F. Van Steen, M. D. Verweij, N. De Jong, J. G. Bosch, and H. J. Vos, “Parasternal versus apical view in cardiac natural mechanical wave speed measurements,” *IEEE Trans. Ultrason. Ferroelectr. Freq. Control* **67**(8), 1590–1602 (2020).